Summit of the East Antarctic Ice Sheet underlain by thick ice-crystal fabric layers linked to glacial–interglacial environmental change

BANGBING WANG[1], BO SUN[2], CARLOS MARTIN[3], FAUSTO FERRACCIOLI[3], DANIEL STEINHAGE[4], XIANGBIN CUI[2] & MARTIN J. SIEGERT[5]*

[1]*Zhejiang University, 38 Zheda Road, Hangzhou, 310027, China*

[2]*Polar Research Institute of China, 451 Jinqiao Road, Pudong, Shanghai, 310026, China*

[3]*British Antarctic Survey, High Cross, Madingley Road, Cambridge CB3 0ET, UK*

[4]*Alfred Wegener Institute Helmholtz Centre for Polar and Marine Research, PO Box 12 01 61, D-27515 Bremerhaven, Germany*

[5]*Grantham Institute and Department of Earth Science and Engineering, Imperial College London, South Kensington, London SW7 2AZ, UK*

**Correspondence: m.siegert@imperial@ac.uk*

Abstract: Ice cores in Antarctica and Greenland reveal ice-crystal fabrics that can be softer under simple shear compared with isotropic ice. Owing to the sparseness of ice cores in regions away from the ice divide, we currently lack information about the spatial distribution of ice fabrics and its association with ice flow. Radio-wave reflections are influenced by ice-crystal alignments, allowing them to be tracked provided reflections are recorded simultaneously in orthogonal orientations (polarimetric measurements). Here, we image spatial variations in the thickness and extent of ice fabric across Dome A in East Antarctica, by interpreting polarimetric radar data. We identify four prominent fabric units, each several hundred metres thick, extending over hundreds of square kilometres. By tracing internal ice-sheet layering to the Vostok ice core, we are able to determine the approximate depth–age profile at Dome A. The fabric units correlate with glacial–interglacial cycles, most noticeably revealing crystal alignment contrasts between the Eemian and the glacial episodes before and after. The anisotropy within these fabric layers has a spatial pattern determined by ice flow over subglacial topography.

Ice sheets contain several types of single ice crystals, such as a perfect single pole, an elongated single pole and a vertical girdle crystal (Fig. 1). Ice crystals experience an anisotropic response to stress, whereby their principal axes, termed C-axes, rotate during deformation towards the direction of compression and away from the tensional direction (Fig. 2; Alley 1988; Azuma *et al.* 1999; Durand *et al.* 2009; Montagnat *et al.* 2014). Collectively, ice-crystal alignment leads to macro-crystallographic orientations, or ice-sheet fabric, which is the product of both ice rheology and stress. As the strain rate in anisotropic ice under simple shear (Azuma 1994; Durand *et al.* 2007; Kennedy *et al.* 2013) can be up to an order of magnitude greater than in isotropic ice (Azuma 1994), a feedback is possible whereby ice fabrics lead to preferential deformation and, in turn, further anisotropy (Alley 1988; Azuma 1994). The spatial variation of ice rheology is fundamental to ice-sheet flow modelling, yet it is normally averaged through depth as an isotropic medium, as in Glen's flow 'law' (Glen 1954). Differences in the velocity of cold-based ice between observations (Thorsteinsson *et al.* 1999) and modelling (Gillet-Chaulet *et al.* 2006; Martin & Gudmundsson 2012), in which respective ice-surface elevations can vary by hundreds of metres, and ice velocities by tens of metres per year, may be attributable to the rheological impacts of ice fabric development. Crystal alignment in ice cores is analysed routinely, revealing marked and step-wise changes in the fabric of ice deposited across glacial–interglacial periods (Durand *et al.* 2007; Montagnat *et al.* 2014). Additionally, sonic logging (Gusmeroli *et al.* 2012) shows how variations in ice-sheet fabric is correlated highly with oxygen isotope ratios, implying a link with atmospheric parameters (Paterson 1991; Kennedy *et al.* 2013). The spatial distribution of ice-sheet fabric is largely unknown, however, as ice cores are heavily restricted in number and distribution across Antarctica and Greenland. As a consequence, the crystallographic structure of ice in large ice sheets,

From: Siegert, M. J., Jamieson, S. S. R. & White, D. A. (eds) 2018. *Exploration of Subsurface Antarctica: Uncovering Past Changes and Modern Processes*. Geological Society, London, Special Publications, **461**, 131–143.
First published online May 26, 2017, https://doi.org/10.1144/SP461.1

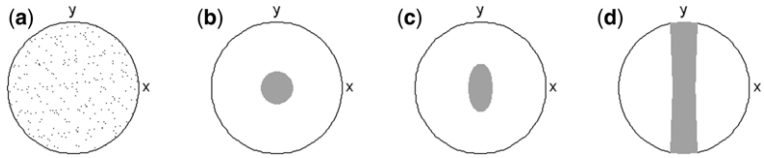

Fig. 1. Schmidt diagrams demonstrating typical fabrics in ice sheets. The fabric can be identified by the difference in permittivity recorded between the primary axes. The axes x and y represent the horizontal plane, and z is vertical. (**a**) Random ice fabric. (**b**) A perfect single pole. (**c**) An elongated single pole. (**d**) A vertical girdle. The perfect single pole and vertical girdle can be considered as the two extremes (end members) of ice fabric under stress-induced deformation, and the elongated single pole is a transient state between changes in stress or shear.

including its development through time and space, and its potential rheological consequences, remains uncertain.

Dome A is the highest ice divide on the East Antarctic Ice Sheet (Jouzel & Masson-Delmotte 2010), with surface elevations reaching over 4100 m above sea-level. During the 2007–09 period of the International Polar Year the Dome A summit region was surveyed by an ice-penetrating polarimetric radar (Sun *et al.* 2009; Fig. 3). Initial inspection of the non-polarized radar data revealed the first detailed images of the Gamburtsev Subglacial Mountains, which were found to contain well-preserved upland glacial geomorphological features and a clearly defined water drainage pattern originating from fluvial activity in preglacial times (Sun *et al.* 2009). Numerical ice-flow modelling suggests these mountains were the nucleation site of the East Antarctic ice sheet, and are likely therefore to have been continuously glaciated for at least 14 Ma (DeConto & Pollard 2003).

Because radio-waves reflect off ice fabrics as a function of orientation, polarimetric radars, which measure radio-wave reflections simultaneously in orthogonal axes, are able to detect gross levels of ice-crystal orientations. Here, we analyse polarimetric data from the Dome A radar survey, revealing insights into the deep-ice crystal structure at and around the ice divide, and its relation with subglacial topography. By linking the data stratigraphically to the Vostok ice core, using airborne radar data, we also provide an assessment of the temporal evolution of ice fabric.

Typical fabrics in ice sheets

Deep ice cores, and some laboratory measurements confirm a direct association between ice-fabric changes and their permittivity (Matsuoka *et al.* 1997; Fujita *et al.* 2000, 2006; Drews *et al.* 2012). Figure 1 and Table 1 show the usual fabric types and their permittivity tensors. Electric permittivity is a measure of how an electric field affects, and is affected by, a dielectric medium. In tri-dimensional anisotropic media, the permittivity is a tensor relating the three components of the electric displacement with those of the electric field. The permittivity tensor can be expressed as a diagonal tensor, as follows:

$$\bar{\varepsilon} = \begin{bmatrix} \varepsilon_1 & 0 & 0 \\ 0 & \varepsilon_2 & 0 \\ 0 & 0 & \varepsilon_3 \end{bmatrix} \quad (1)$$

We assume here that $\varepsilon_1 \leq \varepsilon_2 \leq \varepsilon_3$.

In the case of a random ice-crystal fabric, the response of the electric field within the medium is independent of its orientation and $\varepsilon_1 = \varepsilon_2 = \varepsilon_3$. If $\varepsilon_1 = \varepsilon_2 = \varepsilon_\perp$ and $\varepsilon_3 = \varepsilon_{//}$, an idealized perfect single-pole behaviour occurs (Fig. 1b). For a single-pole ice-fabric distribution, as the ice crystals are aligned in planes, distinct electrical properties will exist along and across those planes. If we denote $\varepsilon_\perp$ and

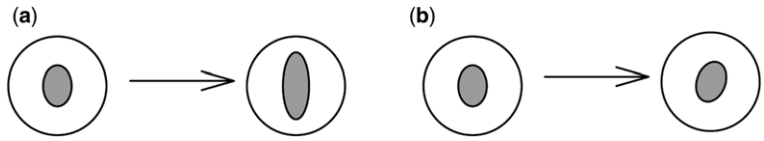

Fig. 2. Schematic diagram of two possible evolutions of an elongated single-pole ice-fabric in 'soft' ice. (**a**) The fabric in the soft (glacial) ice evolves towards a vertical girdle but keeps the same axial orientation as the harder (interglacial) layers. (**b**) The fabric in soft layers rotates faster towards a new stable position as a consequence of flow reorganization. In theory, both can result in a change to the permittivity tensor and hence a change in the echo difference measured by polarimetric radars. The case in (a) is the most common type, as reported in the NEEM, Dome C and Dome Fuji ice cores. Case (b) is theoretical and has yet to be observed directly in the field.

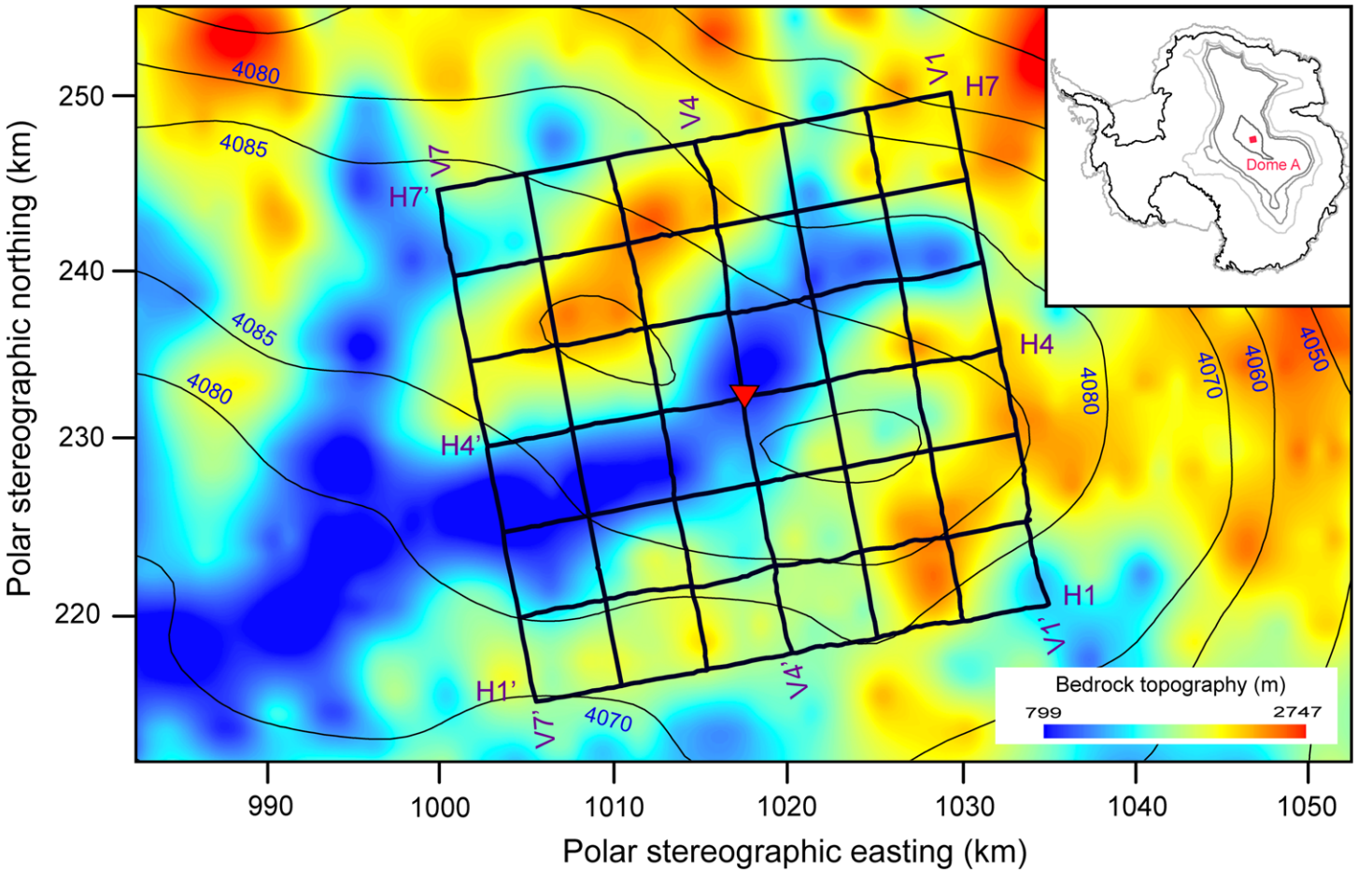

Fig. 3. Location of polarizing radar profiles at Dome A. Orientation of the radar transects superimposed on bed elevation, with ice-surface elevation contours also noted. Red inverted triangle denotes Kunlun station. Individual transects are identified by H1–H7 and V1–V7, referred to in subsequent figures. The location of Dome A is provided in the inset.

Table 1. *The relationship between the typical ice fabric distributions found in ice sheets and their electrical behaviour*

Permittivity in primary axis	Electrical behaviour	Magnitude of component in Figure 1	Type of fabric
$\varepsilon_1=\varepsilon_2=\varepsilon_3$	Isotropy	$\varepsilon_x\cong\varepsilon_y\cong\varepsilon_z$	Random ice (Fig. 1a)
$\varepsilon_1=\varepsilon_2\neq\varepsilon_3$	Uniaxial crystal	$\varepsilon_z>\varepsilon_x, \varepsilon_x\cong\varepsilon_y$	Perfect single pole (Fig. 1b)
		$\varepsilon_x>\varepsilon_y, \varepsilon_y\cong\varepsilon_z$	Vertical girdle (Fig. 1d)
$\varepsilon_1\neq\varepsilon_2\neq\varepsilon_3$	Biaxial crystal	$0<\lvert\varepsilon_x-\varepsilon_y\rvert\ll\lvert\varepsilon_z-\varepsilon_x\rvert$	Elongate single pole (Fig. 1c)

The main components of the permittivity tensor are shown in both the primary axis and in a Cartesian system of coordinates (*x, y, z*), where *z* represents the vertical.

$\varepsilon_{//}$ the permittivity perpendicular and parallel to the normal vector of the crystal planes, respectively, the permittivity tensor can be expressed as $\varepsilon_1=\varepsilon_2=\varepsilon_\perp$ and $\varepsilon_3=\varepsilon_{//}$ (Fig. 1b).

In the case of a vertical girdle fabric, the crystal planes are randomly oriented in a vertical plane. In this situation, the two permittivities are (1) the average between $\varepsilon_\perp$ and $\varepsilon_{//}$ in the vertical plane where fabric is random, and (2) equal to $\varepsilon_{//}$ in the normal direction, as follows: $\varepsilon_2=\varepsilon_3=(\varepsilon_{//}+\varepsilon_\perp)/2$ and $\varepsilon_1=\varepsilon_{//}$ (Fig. 1d).

If the ice crystals have elongated single poles then $\varepsilon_1<\varepsilon_2<\varepsilon_3$ (Fig. 1c). The ellipse ratio in this fabric corresponds to the anisotropy of permittivity in the horizontal direction. The larger this ratio is, the higher the level of anisotropic permittivity.

Polarimetric radio waves and Stokes parameters

Polarimetric radars have orthogonal transmitting and receiving antennas, receiving four series of polarized echo (noted as *HH*, *HV*, *VH* and *VV*). Relative echo powers from these configurations vary through anisotropic media. The classic Stokes vector parameters (referred to below as S_0, S_1, S_2 and S_3) can be used to evaluate and quantify the polarization of such radio-waves as follows.

The Stokes vector parameters, defined by George Gabriel Stokes in 1852, are widely used in electromagnetics and optics for describing the polarization state of electromagnetic radiation, such as its total intensity and degree of polarization and the shape parameters of the polarization ellipse (Stokes 1852; Chandrasekhar 1960; Doake 1981; Mott 2006). As *H* and *V* are orthogonal, we can regard them as axes to build the corresponding Stokes parameters, which can be represented as a vector as follows:

$$S=\begin{bmatrix}S_0\\S_1\\S_2\\S_3\end{bmatrix} \tag{2}$$

Here

$$S_0=|E_H|^2+|E_V|^2 \tag{3}$$

$$S_1=|E_H|^2-|E_V|^2 \tag{4}$$

$$S_2=2\cdot|E_H|\cdot|E_V|\cos\varphi=2\cdot\mathrm{Re}(E_H\cdot E_V) \tag{5}$$

$$S_3=2\cdot|E_H|\cdot|E_V|\sin\varphi=-2\cdot\mathrm{Im}(E_H\cdot E_V) \tag{6}$$

where E_H and E_V are the components of electrical field from the orthogonal receiver antennae; φ is the phase difference between E_H and E_V; and Re and Im are the real and imaginary parts of an electrical field *E*. The normalized Stokes vector parameters can effectively eliminate the influence of transmitting power, antenna interval and so on, and is represented as follows:

$$S'=\begin{bmatrix}1\\S_1/S_0\\S_2/S_0\\S_3/S_0\end{bmatrix} \tag{7}$$

While an electromagnetic wave propagates in an anisotropic media, it can induce both ordinary waves and extraordinary waves in orthogonal directions, each with different propagating velocities. Therefore the incident wave in the *H* or *V* direction can induce reflections both in the same direction and orthogonally. We can describe the relationship of reflection and incident waves as:

$$\vec{E}^{\,r}=\begin{bmatrix}E_H^r\\E_V^r\end{bmatrix}=\bar{R}\cdot\vec{E}^{\,i}=\begin{bmatrix}R_{HH}&R_{HV}\\R_{VH}&R_{VV}\end{bmatrix}\begin{bmatrix}E_H^i\\E_V^i\end{bmatrix} \tag{8}$$

Here, $\vec{E}$ represent the electrical field vector. Its superscript 'i' means that it is the incident wave and 'r' indicates the reflection wave. $\bar{R}$ is a 2×2 reflection coefficient matrix describing the relationship between the incident and reflecting waves.

For induced reflections recorded in the H antenna, we can obtain:

$$\vec{E}^{\mathrm{r}} = \begin{bmatrix} E_H^{\mathrm{r}} \\ E_V^{\mathrm{r}} \end{bmatrix} = \begin{bmatrix} E_{HH} \\ E_{HV} \end{bmatrix} = \begin{bmatrix} R_{HH} & R_{HV} \\ R_{VH} & R_{VV} \end{bmatrix} \begin{bmatrix} E_H^{\mathrm{i}} \\ 0 \end{bmatrix} = \begin{bmatrix} R_{HH} \cdot E_H^{\mathrm{i}} \\ R_{VH} \cdot E_H^{\mathrm{i}} \end{bmatrix} \quad (9)$$

Substituting equation (9) into equation (2), we get the following four relations:

$$S_0 = |E_H^{\mathrm{r}}|^2 + |E_V^{\mathrm{r}}|^2 = |E_H^{\mathrm{i}}|^2 \cdot (|R_{HH}|^2 + |R_{VH}|^2) \quad (10)$$

$$S_1 = |E_H^{\mathrm{r}}|^2 - |E_V^{\mathrm{r}}|^2 = |E_H^{\mathrm{i}}|^2 \cdot (|R_{HH}|^2 - |R_{VH}|^2) \quad (11)$$

$$S_2 = 2 \cdot \mathrm{Re}(E_H \cdot E_V) = 2 \cdot |E_H^{\mathrm{i}}|^2 \cdot |R_{HH}| \cdot |R_{VH}| \cdot \cos(\varphi_H + \varphi_{HH} - \varphi_{VH}) \quad (12)$$

$$S_3 = -2 \cdot \mathrm{Im}(E_H \cdot E_V) = -2 \cdot |E_H^{\mathrm{i}}|^2 \cdot |R_{HH}| \cdot |R_{VH}| \cdot \sin(\varphi_H + \varphi_{HH} - \varphi_{VH}) \quad (13)$$

For inducing reflections measured in the V antenna we obtain similar expressions.

S_0 refers to the total echo-power from the orthogonal antennae, and resembles the reflected power using in the conventional sole-channel radar system. S_1, S_2 and S_3 provide the difference in reflected power between the orthogonal electric fields in the standard Cartesian arrangement, a Cartesian system rotated by 45° and in a circular coordinate arrangement, respectively, thus providing measures of the anisotropy in ice permittivity.

Several authors have confirmed the relationship between the echo difference in orthogonal directions and the permittivity tensor of ice (Hargreaves 1977; Fujita *et al.* 2006; Matsuoka *et al.* 2012), which is linked to the second-order tensor of ice fabric (Matsuoka *et al.* 2009). Hence, in the absence of plausible alternative explanations, it can be assumed that the Stokes vector parameter description of the polarimetric radar reflections S_1, S_2 and S_3 expresses ice-sheet anisotropy caused by ice crystal fabric.

Radar survey

The polarimetric radar used a frequency of 179 MHz and recorded radio waves in orthogonal orientations over a square grid of fourteen 30 km-long transects with along-track sample acquisition every *c.* 17 m (Fig. 3). The radar employed dual receivers in orthogonal orientations (H and V) with a time-sharing sole transmitter (H or V). It comprised four assembly antenna pairs: *HH*, *HV*, *VH* and *VV*. An in-phase/quadrature (I/Q) demodulator can measure the amplitude, phase and instantaneous frequency of radar signals, so it is widely used in polarimetric radar systems. Normally each antenna pair records both I and Q components for detecting phase. Therefore there are eight data records in the polarimetric radar files necessary to measure information of both the amplitude and phase of reflected waves. Further details of the radar are provided in Sun *et al.* (2009).

The I and Q components of the four antenna pairs were imported from raw data files, from which the Stokes vectors of both H and V transmitters were calculated. The four parameters in the Stokes vector each have an explicit physical meaning. S_0 represents the average power of the EM waves. S_1 provides the echo difference between H and V components. Its value can be positive, zero or negative depending on whether linear polarization of H or V is dominating. S_2 provides the echo difference of orthogonal components between 45 and −45°. S_3 represents the echo difference of orthogonal components within a circular coordinate system. After normalization, S_1, S_2 and S_3 all range between −1 and +1.

S_0 has similar results to traditional (non-polarimetric) radar reflections. It can display clear isochrones and subglacial topography. In contrast S_1, S_2 and S_3 display obvious bands within the normal isochrone arrangements (e.g. red (positive) and blue (negative) layers in Fig. 4). The units in S_1 and S_2 are more distinct than in S_3 and show little difference between the H and V transmitters. By adding S_0, S_1 and the average power from H and V together, the positive layers link to reflections recorded in the V component, and the negative layers link to the H component. If the coordinates are fixed (i.e. as in a straight survey line), variation of the Stokes vectors in the H and V components within different layers of ice must be attributed to differences in the ice crystal fabric (i.e. different layers have different fabric and orientation tensors).

The Stokes vectors were calculated in each of the transects (Fig. 4), revealing four obvious englacial layered units in which discrete variations in S_1 were noticed, named T_1, T_2, T_3 and T_4, respectively (T_0 designates the bed). Beneath T_4, further units of alternating S_1 occur, but they are less obvious and not as easy to trace owing to the lack of returned power from deeper englacial reflectors. Broadly, positive S_1 units (red–yellow zones in Fig. 4) correspond to high levels of anisotropy in the horizontal plane (as the radar is insensitive to the anisotropy

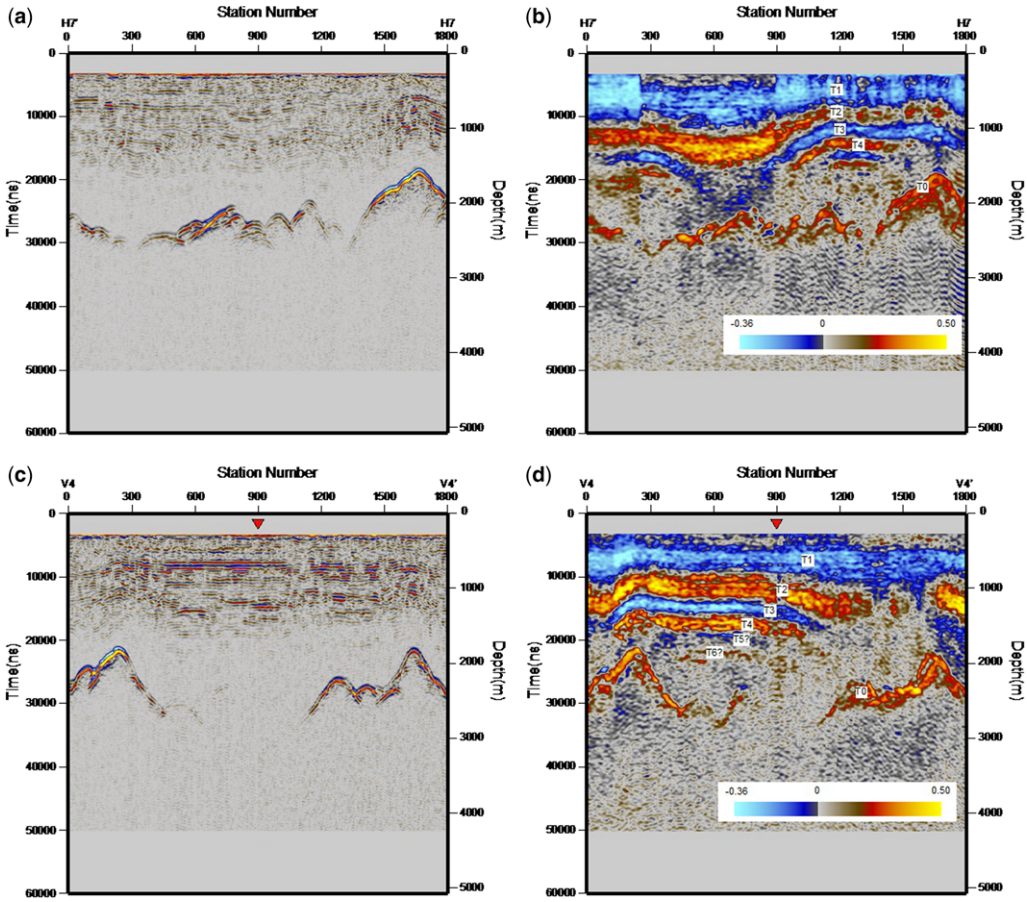

Fig. 4. The radar images of lines H7 and V4. (**a**, **c**) The S_0 cross-section (Z scopes) of H7 and V4 lines derived from the Stokes vector. (**b**, **d**) The corresponding S_1measurements, revealing ice-sheet anisotropic variations. Units T_1–T_4 refer to ice fabric units (discussed in the text) and T_0 is the bed reflector. The locations of H7 and V4 are provided in Figure 3. The red inverted triangle V4 denotes Kunlun station, as in Figure 3.

in the direction of transmission), and negative S_1 units (blue zones) are derived from either isotropic ice or low levels of anisotropy in the horizontal plane. As expected, the deeper S_1 ice fabric units thin gradually with depth owing to vertical compression (Fig. 4). Unit T_1 is the thickest of those measured, from the surface to ice depths of *c.* 800–1000 m. Based on crystallographic information from deep ice cores, this upper unit will have a nearly random (isotropic) fabric (Azuma 1994; Azuma *et al.* 1999; Fujita *et al.* 2006; Durand *et al.* 2009; Montagnat *et al.* 2014). Unit T_2 (positive S_1) is up to *c.* 400 m thick and contains an abundance of highly anisotropic ice related to a vertical girdle fabric distribution. T_3 (negative S_1) is a product of low levels of horizontal anisotropy, as the fabric clusters towards a broad single-pole distribution (Hargreaves 1977; Eisen *et al.* 2007; Matsuoka *et al.* 2009). T_4 (highly positive S_1) is similar in crystal arrangement to T_2. While both the thickness and depth of the units fluctuate horizontally substantially, we estimate that *c.* 20% of the ice column beneath Dome A, and up to *c.* 50% of the ice column at depths >1 km around this ice dome, are characterized by high levels of anisotropy (primarily from T_2, T_4 and T_6; Fig. 4).

Dating fabric units

Link to Vostok ice core

We are able to link radar isochrones from Kunlun Station to the Vostok ice core, allowing us to estimate a depth–age relationship at Dome A (Figs 5 & 6). The depth of the ice fabric units at Kunlun is then used to assign estimated ages to the fabric units (Table 2). We also used the stratigraphic

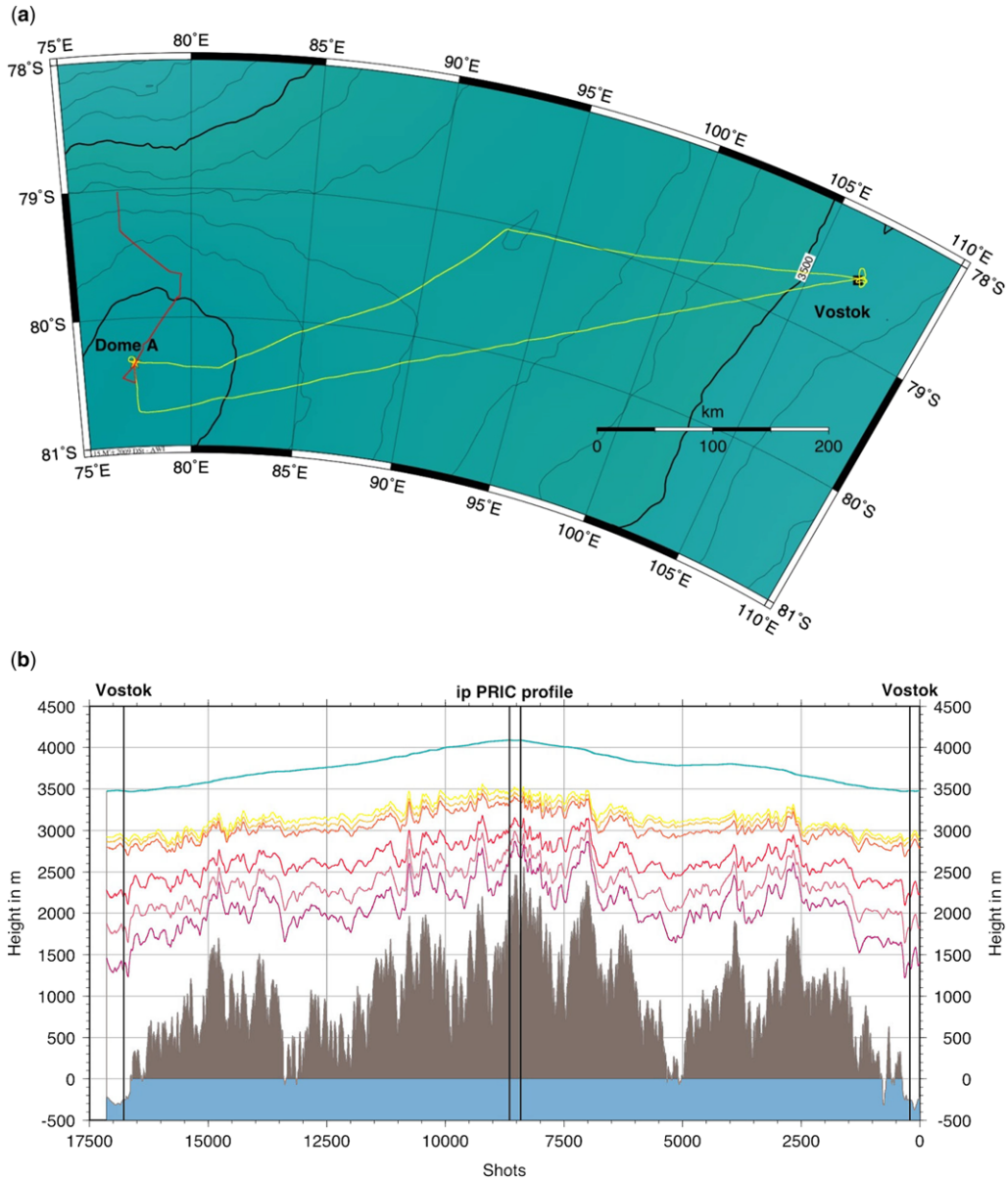

Fig. 5. Radar transect and internal layers between Vostok Station and Kunlun Station at the summit of Dome A. (**a**) Map of radar profiles. The transects yielded well-resolved RES data, from which internal layers between the stations were traced. Ice surface elevation contours at intervals of 100 m are provided. (**b**) Traced internal layers along the profiles given in (a), so revealing the depth–age relationship at Kunlun Station (Fig. 6).

connection to Vostok to translate the ice core dust and ΔT records to Dome A (Fig. 7).

Isochrone layers were picked along two airborne radar transects, collected by the Alfred Wegener Institute. The radar used operates at 150 MHz, alternating between 600 and 60 ns bursts, with internal stacking of shots prior to storage and a pulse repetition frequency of 20 Hz. The effective distance between 60 ns shots is *c.* 8 m, and for interpretation the shots are stacked two-fold (so that *c.* 8 m becomes *c.* 16 m). The two-way travel times of the layers were converted into ice depth using the Kovacs formula (Kovacs *et al.* 1995) and ice density information (Barkov 1970; Ekaykin *et al.* 2010),

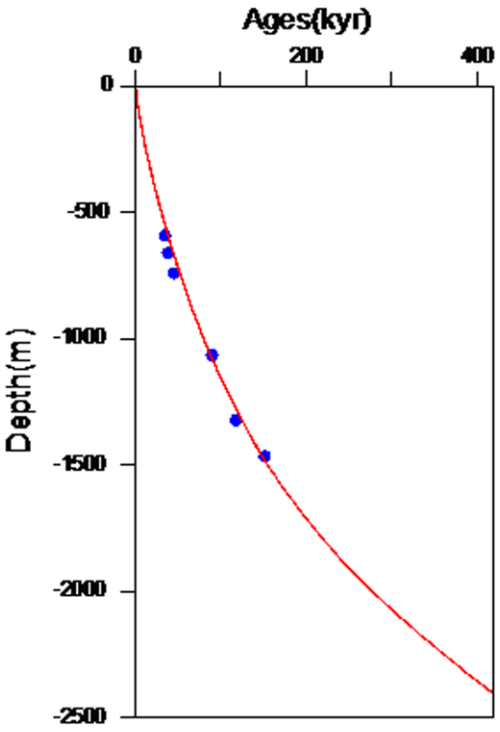

Fig. 6. Depth–age curve at the Dome A summit. The blue points denote the age–depth data from dated radar internal horizons tracked from the Vostok ice core site (Fig. 5). The line is the 'best-fit' (polynomial) curve to the data points, and serves as an approximate depth–age relationship at Dome A.

with an accuracy of *c.* 5%. The radar data were differentiated and amplitude balanced to aid the extraction of the layers. The age–depth relationship at Vostok Station was taken from Parrenin *et al.* (2004). The layers were traced using a commercial software package from Landmark, which displays picked horizons at cross-over points and thus allows an evaluation the quality of the data to ensure the correct isochrone is identified along the transect. Importantly, layers were traced along both transects from Dome A and compared at their intersection at Vostok Station. Agreement between the layers at Vostok Station provides confidence that the correct layers were followed to Dome A, and that the depth–age relationship there is reliable. The error for picking both the ice-surface reflection and an isochrone is about five sample points, which corresponds to 66.65 ns or *c.* 5.6 m in ice thickness.

Ages of fabric layers

From the stratigraphic correlation between Vostok and Dome A, we estimate that the base of T_2 is *c.* 105 kyr, which roughly corresponds with the end of the Eemian interglacial period. T_3 is aged between *c.* 105 and *c.* 136 kyr, and there is a good correspondence between the peak of S_1 within T_3 and the peak of the Eemian. T_4 is between *c.* 136 and *c.* 190 kyr, similar to MIS 6. Two faint units below T_4, named T_5 and T_6, are possibly consistent with previous glacial/interglacial periods.

Broadly, positive S_1 units (T_2, T_4) correspond well to glacial periods and negative S_1 units (T_3, T_5) are associated with interglacials (Fig. 7). This suggests that gross crystal fabric across Dome A is influenced by past environmental change at the glacial–interglacial transition.

Crystal fabrics at Dome A: distribution and significance

In a vertical column of ice near the ice divide, the orientation of ice crystals will gradually tend to a predominant (vertical) orientation under compression. In doing so, the ice fabric develops from 'random' to 'single pole'. Horizontally, perfect single pole and 'vertical girdle' crystal alignments represent the two end-member extreme fabrics (Figs 1 & 2a) that could be expected in idealized ice-divide and ice-sheet margin regions, respectively. The resulting development of ice fabric in layers T_1–T_5 is illustrated in Figure 8. An alternative, theoretical, explanation is that under shear the crystal axis experiences rotation in line with the stress field (Fig. 2b). Both

Table 2. *Ice fabric layer depths and their ages at Kunlun Station*

Fabric layers	Radar travel time (ns)	Ice depth (m)	Age (kyr)	Period
T_1	956	807.3	0–57	Holocene and Late Wisconsin
T_2	1452	1226.2	57–106	Early Wisconsin
T_3	1657	1399.3	106–135	Eemian
T_4	1952	1648.4	135–190	
T_5?	2206	1862.9	190–240	
T_6?	2429	2051.3	240–296	

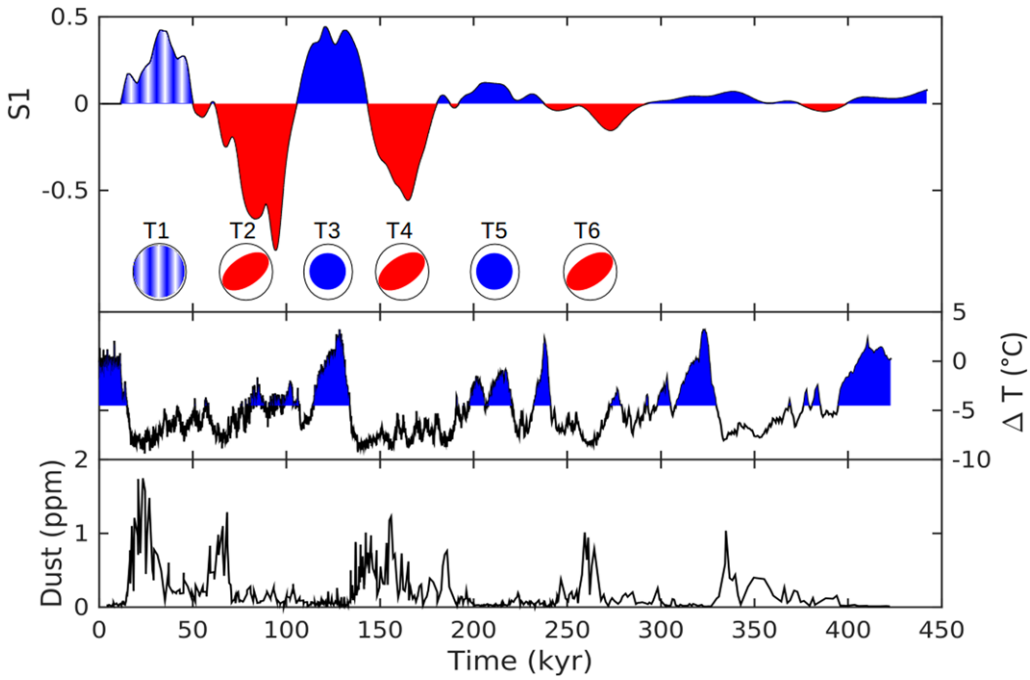

Fig. 7. Comparison between ice fabric units and the Vostok dust and ΔT records. We construct a new age–depth relation at Dome A by dating radar internal horizons by tracking them from Kunlun Station to the Vostok ice core site (Fig. 6). T_2–T_4 refer to the same fabric units as presented in Figure 4d. T_5 and T_6 are deeper units, and because both are faint we can only infer approximate ages.

explanations, summarized in Table 3, would yield similar polarimetric radar measurements.

It is known that soft layers (glacial ice) are more easily deformed under stress than hard layers (interglacial ice) and isotropic ice (e.g. Paterson 1991; Thorsteinsson *et al.* 1999; Durand *et al.* 2007; Matsuoka *et al.* 2012; Kennedy *et al.* 2013). The deformation leads to the glacial ice layers more easily experiencing crystal realignment (Fig. 2a), which is what is recorded by the Stokes vectors measurements (Fujita *et al.* 2006; Wang *et al.* 2008; Matsuoka *et al.* 2012). Hence, the polarimetric radar

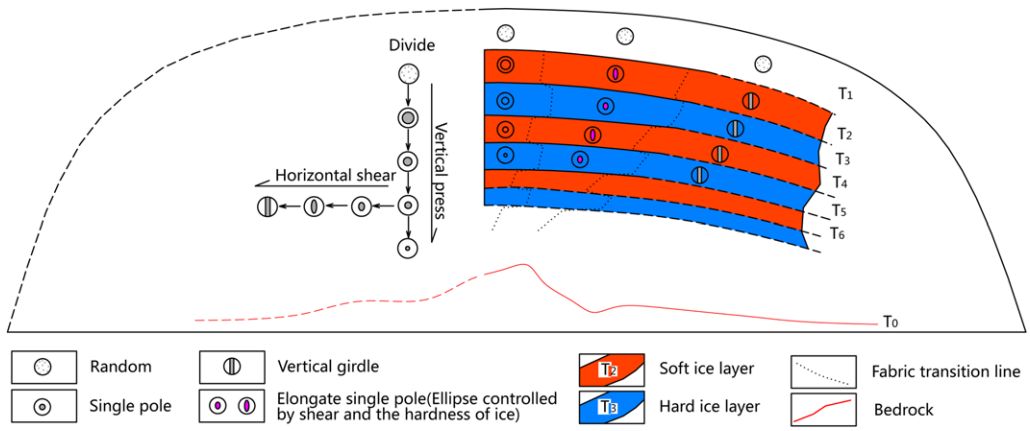

Fig. 8. Conceptual model for the development of ice-sheet fabric within layers of soft (glacial) and hard (interglacial) ice over and near an ice divide.

Table 3. *Proposed dominant crystal fabrics at Dome A, following two possible crystal evolutions illustrated in Figure 2*

Layer	Option a in Figure 2	Option b in Figure 2
T_1	O	O
T_2	/	/
T_3	o	\
T_4	/	/
T_5	o	\

Symbols are as follows: O = isotropic; / and \ = elongate single pole or vertical girdle in different horizontal directions; and o = single pole.

measures the thickness and distribution of layers with discrete ice fabrics.

The S_1 units align well among the individual transverses and cross profiles. We picked the top and bottom surfaces of all the S_1 units in each line (where S_1 became 0) to make three-dimensional wall and surface diagrams (Fig. 9), which display the extent and thickness of each fabric horizon revealing two obvious features. The first is significant S_1 variations in both ice depth and unit thickness. The second is changes to ice fabric caused by flow over macro-scale bed topography (Robin & Millar 1982). The fabric units are dominant across the left side of a major subglacial valley. On the right side of the subglacial valley, a cluster of relatively small peaks exists. Unit T_2 pinches out immediately above these peaks (Fig. 9). In this area, an arcuate belt with no S_1 signal covers the cluster of peaks. We infer that, above these smaller peaks, a pure compressive stress state (uniaxial or pure shear) dominates, causing the fabric to be characterized by a single-pole arrangement (Azuma 1994; Matsuoka *et al.* 2012). This induces isotropy in the horizontal direction, causing the S_1 to be near zero (*c.* 25 km mark in Fig. 4d), leading to local disappearance of the fabric units. Away from the peaks, simple shear will increase gradually, leading to the redevelopment of fabric units that can be seen on both sides (Fig. 9d).

Our polarimetric radar data reveal widespread ice-sheet anisotropy at Dome A. However, polarimetric radar only captures relative contrasts in electric permittivity between two orthogonal directions in the horizontal plane rather than the actual values. Interpretation of our radar data has been guided by typical ice-fabric distributions sampled in ice cores sites (e.g. Durand *et al.* 2007 at Dome C; Drews *et al.* 2012 at EPICA DML; and Montagnat *et al.* 2014 at NEEM). Ice-core data only show subtle changes in fabric during climatic transitions, however, in contrast with the marked transitions we image in radar data. This suggests that widespread but locally subtle transitions in ice fabric are likely to have a large effect on the permittivity of the ice sheet. Hence subtle transitions in ice fabric could potentially have a larger effect on ice flow dynamics than currently considered.

Our observations at Dome A are likely to hold for other ice divides, including central Greenland, as noted above. At Dome F in East Antarctica, using a dual frequency radar, simple-shear-dominated ice flow over large subglacial obstacles has been shown to lead to preferential recrystallization along bands of relatively soft ice (Fujita *et al.* 1999), meaning that the rheological consequences of initial anisotropy will evolve downstream. At Dome C, Siegert & Fujita (2001) analysed 60 MHz radar, and discovered that the form of the depth-to-power relationship of the returned radar signal could be used as a proxy for the along-track development of ice-crystal fabric. A similar investigation revealed how ice fabric may evolve between Ridge B and Lake Vostok (Siegert & Kwok 2000).

One situation where the downstream modification to ice crystal fabric and rheology may be highly relevant is in the preservation of major blocks of basal ice, interpreted to be caused by widespread and thick basal accretion (Bell *et al.* 2011). Stress-induced anisotropy-may lead to preferential englacial flow along bands, leading to smooth englacial flow over rough topography and, potentially, a partial flow 'decoupling' of the bulk of the ice sheet from basal ice units frozen to the bed. This new and alternative explanation for the so-called 'accretion ice' identified atop the Gamburtsev Subglacial Mountains (and other 'fuzzy' lower-englacial features seen in both Greenland and Antarctica) is consistent with the lack of significant surface uplift and velocity anomalies that a high rate of basal freezing (of the order of the surface rate of ice accumulation) should lead to, and is consistent with meteoric radar layering above the basal ice that drapes smoothly over it (see Wrona *et al.* 2017). Such flow may preserve the basal ice units as ancient ice blocks, which means that the rate of ice accumulation by freezing will be lower, and the age of ice considerably older (possibly by millions of years), than first thought.

Conclusions and further work

Polarimetric radar measurements, linked stratigraphically to the Vostok ice core, demonstrate that ice-sheet crystal alignment at the centre of large ice sheets is a function of both climate-induced impurities acting to 'soften' the ice during periods of glaciation and internal stresses within the ice sheet, acting to preferentially deform the soft ice, yielding ice-sheet anisotropy. These observations at and around Dome

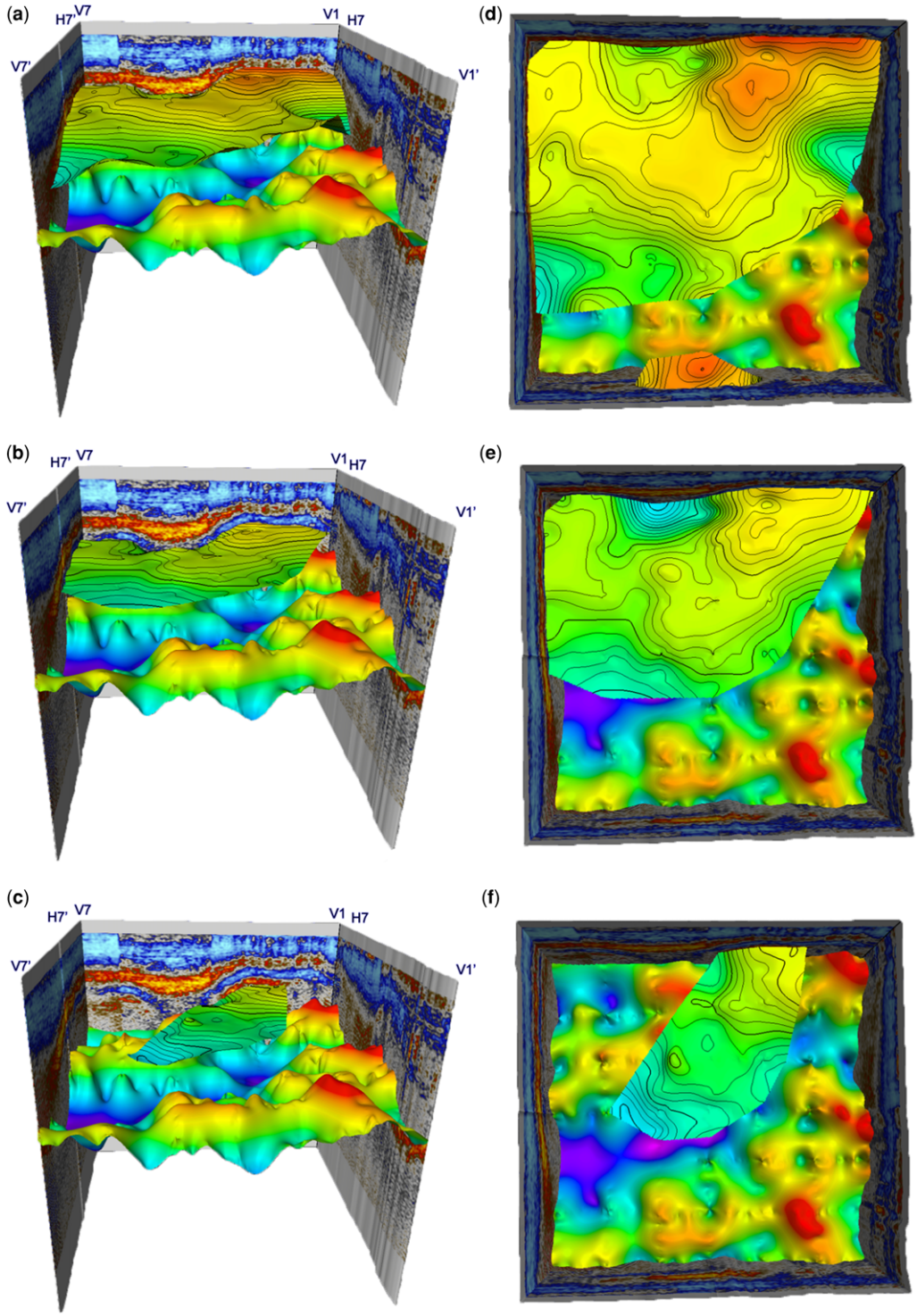

Fig. 9. Three-dimensional visualization of T_2, T_3 and T_4 fabric units and their relationship to the ice-sheet bed. (**a**, **d**) T_2; (**b**, **e**) T_3; and (**c**, **f**) T_4 (see Table 3).

A are likely to hold for other ice divides, including central Greenland, where soft anisotropic ice has been measured in the lower portion of the NEEM ice core (NEEM Community Members 2013).

The next steps to this area of research are two-fold: first, to study ice crystal fabric developments using polarimetric radar around other ice divides, to understand the similarities to, and differences from, the situation at Dome A; and second, to investigate the degree to which the ice fabric uncovered at Dome A relates to modification in ice rheology. Ice-sheet modelling is capable of such analysis, through assimilation of three-dimensional internal layer structures into the ice flow parameter. This coupling between data and modelling is possible, but requires high-resolution radar data acquisition across study regions.

This paper is based on the work supported by the National Natural Science Foundation of China (40874060, 41176167, 41276200 and 41676181), the 973 projects of China (2012CB957702), the 863 projects of China (2011AA040202) and the UK Natural Environment Research Council (NE/D003733/1). This work was carried out while Bangbing Wang was a visiting research fellow at the British Antarctic Survey. We thank Richard Hindmarsh, Hugh Corr and Ed King for help and advice in developing the work for this paper. We also thank Neil Ross and Adam Booth for offering constructive and helpful reviews.

References

ALLEY, R.B. 1988. Fabrics in polar ice sheets: development and prediction. *Science*, **240**, 493–495.

AZUMA, N. 1994. A flow law for anisotropic ice and its application to ice sheets. *Earth and Planetary Science Letters*, **128**, 601–614.

AZUMA, N., WANG, Y., MORI, K., NARITA, H., HONDOH, T., SHOJI, H. & WATANABE, O. 1999. Textures and fabrics in the Dome F (Antarctica) ice core. *Annals of Glaciology*, **29**, 163–168.

BARKOV, N.I. 1970. Preliminary results of ice sheet drilling at Vostok Station. *Soviet Antarctic Expedition, Information Bulletin*, **80**, 24–29 [in Russian].

BELL, R.E., FERRACCIOLI, F. *ET AL.* 2011. Widespread persistent thickening of the East Antarctic ice sheet by freezing from the base. *Science*, **331**, 1592–1595.

CHANDRASEKHAR, S. 1960. *Radiative Transfer*. Dover, New York.

DECONTO, R.M. & POLLARD, D. 2003. Rapid Cenozoic glaciation of Antarctica induced by declining atmospheric CO_2. *Nature*, **421**, 245–249.

DOAKE, C.S.M. 1981. Polarization of radio waves in ice sheets. *Geophysical Journal of the Royal Astronomical Society*, **64**, 539–558.

DREWS, R., EISEN, O., STEINHAGE, D., WEIKUSAT, I., KIPFSTUHL, S. & WILHELMS, F. 2012. Potential mechanisms for anisotropy in ice-penetrating radar data. *Journal of Glaciology*, **58**, 613–624.

DURAND, G., GILLET-CHAULET, F. *ET AL.* 2007. Change in ice rheology during climate variations-implications for ice flow modeling and dating of the EPICA Dome C core. *Climate of the Past*, **3**, 155–167.

DURAND, G., SVENSSON, A. *ET AL.* 2009. Evolution of the texture along the EPICA dome C ice core. *Low Temperature Science* (Supplement Issue: Physics of Ice Core Records II. Institute of Low Temperature Science, Hokkaido University, Sapporo Japan), **68**, 91–106.

EISEN, O., HAMANN, I., KIPFSTUL, S., STEINHAGE, D. & WILHELMS, F. 2007. Direct evidence for continuous radar reflector originating from changes in crystal-orientation fabric. *The Cryosphere*, **1**, 1–10.

EKAYKIN, A.A., LIPENKOV, V.Y., PETIT, J.R., JOHNSEN, S., JOUZEL, J. & MASSON-DELMOTTE, V. 2010. Insights into hydrological regime of Lake Vostok from differential behavior of deuterium and oxygen-18 in accreted ice. *Journal of Geophysics Research*, **115**, C05003, 1–14. https://doi.org/10.1029/2009JC005329

FUJITA, S., MAENO, H., URATSUKA, S., FURUKAWA, T., MAE, S., FUJII, Y. & WATANABE, O. 1999. Nature of radio echo layering in the Antarctic ice sheet detected by a two frequency experiment. *Journal of Geophysics Research*, **104**, 13,013–13,024.

FUJITA, S., MATSUOKA, T., LSHIDA, T., MATSUOKA, K. & MAE, S. 2000. A summary of the complex dielectric permittivity of ice in the megahertz range and its application for radar sounding of polar ice sheets. *In*: HONDOH, T. (ed.) *Physics of Ice Core Records*. Hokkaido University Press, Sapporo, Japan, 185–212.

FUJITA, S., MAENO, H. & MATSUOKA, K. 2006. Radio-wave depolarization and scattering within ice sheets: a matrix-based model to link radar and ice-core measurements and its application. *Journal of Glaciology*, **52**, 407–424.

GILLET-CHAULET, F., GAGLIARDINI, O., MEYSSONNIER, J., ZWINGER, T. & RUOKOLAINEN, J. 2006. Flow-induced anisotropy in polar ice and related ice-sheet flow modeling. *Journal of Non-Newtonian Fluid Mechanics*, **134**, 33–43.

GLEN, J.W. 1954. The creep of polycrystalline ice. *Proceedings of the Royal Society, London A*, **A228**, 519–538.

GUSMEROLI, A., PETTIT, E., KENNEDY, J. & RITZ, C. 2012. The crystalline fabric of glacial ice from full-wave borehole sonic logging. *Journal of Geophysics Research*, **117**, 1–13.

HARGREAVES, N.D. 1977. The polarization of radio signals in radio echo sounding of ice sheets. *Journal of Physics D: Applied Physics*, **10**, 1285–1304.

JOUZEL, J. & MASSON-DELMOTTE, V. 2010. Deep ice cores: the need for going back in time. *Quaternary Science Review*, **29**, 3683–3689, https://doi.org/10.1016/j.quascirev.2010.10.002

KENNEDY, J.H., PETTIT, E.C. & DI PRINZIO, C.L. 2013. The evolution of crystal fabric in ice sheets and its link to climate history. *Journal of Glaciology*, **59**, 357–373.

KOVACS, A., GOW, A.J. & MOREY, R.M. 1995. The in-situ dielectric constant of polar firn revisited. *Cold Regions Science and Technology*, **23**, 245–256.

MARTIN, C. & GUDMUNDSSON, G.H. 2012. Effects of nonlinear rheology, temperature and anisotropy on the relationship between age and depth at ice divides. *The Cryosphere*, **6**, 1221–1229.

MATSUOKA, K., WILEN, L., HURLEY, S.P. & RAYMOND, C.F. 2009. Effects of birefringence within ice sheets on obliquely propagating radio waves. *IEEE Transactions on Geoscience and Remote Sensing*, **47**, 1429–1443.

MATSUOKA, K., POWER, D., FUJITA, S. & RAYMOND, C.F. 2012. Rapid development of anisotropic ice-crystal-alignment fabrics inferred from englacial radar polarimetry, central West Antarctica. *Journal of Geophysics Research*, **117**, F03029, https://doi.org/10.1029/2012JF002440

MATSUOKA, T., FUJITA, S. & MAE, S. 1997. Dielectric properties of ice containing ionic impurities at microwave frequencies. *Journal of Physical Chemistry B*, **101**, 6219–6222.

MONTAGNAT, M., AZUMA, N. *ET AL.* 2014. Fabric measurement along the NEEM ice core, Greenland, and comparison with GRIP and NGRIP ice cores. *The Cryosphere*, **8**, 1129–1138, https://doi.org/10.5194/tc-8-1129-2014

MOTT, H. 2006. *Remote Sensing with Polarimetric Radar*. John Wiley & Sons, Hoboken, NJ.

NEEM COMMUNITY MEMBERS 2013. Eemian interglacial reconstructed from a Greenland folded ice core. *Nature*, **493**, 489–494.

PARRENIN, F., RÉMY, F., RITZ, C., SIEGERT, M.J. & JOUZEL, J. 2004. New modelling of the Vostok ice flow line and implication for the glaciological chronology of the Vostok ice core. *Journal of Geophysics Research*, **109**, https://doi.org/10.1029/2004JD004561

PATERSON, W.S.B. 1991. Why ice-age ice is sometimes 'soft'. *Cold Regions Science and Technology*, **20**, 75–98.

ROBIN, G. DE.Q. & MILLAR, D.H.M. 1982. Flow of ice sheets in the vicinity of subglacial peaks. *Annals of Glaciology*, **3**, 290–294.

SIEGERT, M.J. & FUJITA, S. 2001. Internal ice-sheet radar layer profiles and their relation to reflection mechanisms between Dome C and the Trans Antarctic Mountains. *Journal of Glaciology*, **47**, 205–212.

SIEGERT, M.J. & KWOK, R. 2000. Ice-sheet radar layering and the development of preferred crystal orientation fabrics between Lake Vostok and Ridge B, central East Antarctica. *Earth and Planetary Science Letters*, **179**, 227–235.

STOKES, G.G. 1852. On the change of refrangibility of light. *Philosophical Transactions of the Royal Society, London*, **142**, 463–562, https://doi.org/10.1098/rstl.1852.0022

SUN, B., SIEGERT, M.J. *ET AL.* 2009. The Gamburtsev Mountains and the origin and early evolution of the Antarctica ice sheet. *Nature*, **459**, 690–693.

THORSTEINSSON, T., WADDINGTON, E.D., TAYLOR, K.C., ALLEY, R.B. & BLANKENSHIP, D.D. 1999. Strain-rate enhancement at Dye 3. Greenland. *Journal of Glaciology*, **45**, 338–345.

WANG, B.B., TIAN, G., CUI, X. & ZHANG, X. 2008. The internal COF features in Dome A of Antarctica revealed by multi-polarization-plane RES. *Applied Geophysics*, **5**, 230–237.

WRONA, T., FERRACCIOLI, F., CORR, H., WOLOVICK, M. & SIEGERT, M.J. 2017. Reinspection of englacial layering across the Gamburtsev Mountains, East Antarctica. *In*: SIEGERT, M.J., JAMIESON, S.S.R. & WHITE, D.A. (eds) *Exploration of Subsurface Antarctica: Uncovering Past Changes and Modern Processes*. Geological Society, London, Special Publication, 461.